Engineering Structures 343 (2025) 121046

Contents lists available at ScienceDirect

Engineering Structures

journal homepage: www.elsevier.com/locate/engstruct

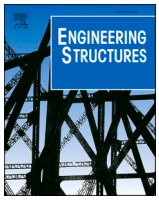

Machine learning-based framework for rapid assessment of seismic resilience and sustainability metrics for regional RC bridges

Zhijian Qiu [a,b], Xiao Li [a], Zilan Zhong [b], Yewei Zheng [c,*]

[a] School of Architecture and Civil Engineering, Xiamen University, Xiamen, Fujian 361005, China
[b] The Key Laboratory of Urban Security and Disaster Engineering of the Ministry of Education, Beijing University of Technology, Beijing 100124, China
[c] School of Civil Engineering, Wuhan University, Wuhan, Hubei 430072, China

ARTICLE INFO

Keywords:
Resilience
Sustainability
RC bridges
PBEE
ANN
Finite element

ABSTRACT

The seismic resilience and environmental impact of reinforced concrete (RC) bridges during earthquakes are crucial for maintaining the functionality and sustainability of transportation networks in earthquake-prone regions. This study presents a machine learning (ML)-based framework that integrates performance-based earthquake engineering (PBEE) principles and ML models to rapidly assess seismic resilience and post-earthquake losses, including repair time, repair costs, and sustainability metrics quantified by carbon footprint, for regional RC bridges. Based on twelve bridge key attributes, including column height and diameter, 1000 finite element (FE) bridge models are systematically developed through the Latin Hypercube Sampling (LHS) method and subjected to 100 ground motions to compute probabilistic seismic demand models, system-level fragility, seismic resilience, and post-earthquake losses. Through hyperparameter tuning and *k*-fold cross-validation, six ML models are optimized with the artificial neural network (ANN) achieving superior accuracy in predicting seismic resilience. Subsequently, the developed ANN framework is applied to representative regional RC bridges, facilitating rapid and reliable predictions of seismic resilience and post-earthquake losses across varying bridge attributes. Overall, the developed framework serves as an efficient and practical tool for decision-makers, providing valuable insights to enhance seismic resilience and sustainability metrics while optimizing post-earthquake recovery strategies for critical infrastructure.

1. Introduction

Reinforced concrete (RC) bridges are essential components of transportation networks, playing a crucial role in ensuring connectivity and efficient mobility. However, strong earthquakes can severely damage these RC bridges, resulting in significant economic losses and environmental impacts during the post-earthquake recovery. Such consequences are observed in past events, including the 1999 Chi-Chi earthquake [35], the 2008 Wenchuan earthquake [27], the 2010 Maule earthquake [56], the 2011–2012 Christchurch earthquake [17] and the 2021 Maduo earthquake [63]. Consequently, rapid and accurate assessment of RC bridge seismic performance is essential for improving resilience, guiding recovery and retrofit efforts, and ensuring effective emergency management [2,24,61].

Resilience is defined as the ability of structures, infrastructure, or communities to withstand extreme events and efficiently restore functionality while minimizing disruption [28,8]. Currently, the seismic resilience assessment framework [13,18] has been extensively applied to various infrastructure systems to evaluate their performance and recovery under seismic hazards, including bridges [19,48,61]. A large number of studies have further extended this framework to account for the effects of material and structural deterioration in RC bridges [12,29,3,33,46,49,66]. For instance, Biondini et al. [7] developed a probabilistic framework for evaluating the life-cycle seismic resilience of a continuous RC bridge exposed to chloride-induced corrosion, while Zhou et al. [65] assessed the seismic resilience of a coastal RC bridge under combined effects of scour and uniform corrosion. More recently, Forcellini and Mitoulis [23] introduced a framework that integrates material deterioration into bridge seismic resilience assessments, revealing its significant impact on repair costs and recovery time.

With the rapid advancement of computational technologies, machine learning (ML) methods have been extensively applied at various scales, from individual bridges to bridge portfolios and bridge-road networks. As such, to improve the accuracy of seismic assessments, a

* Corresponding author.
E-mail address: yzheng@whu.edu.cn (Y. Zheng).

https://doi.org/10.1016/j.engstruct.2025.121046
Received 21 March 2025; Received in revised form 22 June 2025; Accepted 23 July 2025
Available online 30 July 2025

large number of studies have been conducted, including seismic demand prediction, damage or fragility evaluation and resilience assessment [1,10,20,31,32,39,41,40,5,51,53,58,59,62,64,66]. For instance, Soleimani and Liu [54] developed an ANN-based PSDM to improve prediction accuracy and support bridge fragility assessments. Mangalathu et al. [40] proposed a ML-based approach for rapid bridge damage state assessment using bridge-specific attributes. Liu et al. [34] introduced an ANN method for seismic fragility analysis of multi-span bridges, offering a faster alternative to traditional incremental dynamic analysis.

Expanding upon the pioneering studies [18,59,65], this study presents a ML-based framework that integrates performance-based earthquake engineering (PBEE) principles [4,36,38,49] and ML models to enhance the rapid assessment of seismic resilience and post-earthquake losses, including repair time, repair costs, and sustainability metrics quantified by carbon footprint, for regional RC bridges under earthquakes. As sustainability becomes a pressing concern in infrastructure development [15,30,43,44,55], the inclusion of environmental impacts and life-cycle costs within ML-based frameworks proves crucial for optimizing bridge performance and supporting informed, sustainable decision-making.

2. Machine learning-based framework for regional RC bridges

Fig. 1 illustrates the developed ML-based framework for predicting seismic resilience and post-earthquake losses, including repair cost, carbon footprint, and repair time, for regional RC bridges subjected to seismic events. The framework consists of four main steps:

i) Key bridge attributes, including geometric parameters (e.g., column height, column diameter, and span length) and material properties (e.g., concrete compressive strength and steel yield strength), are first collected to represent the variability within regional RC bridge inventories. Based on these attributes, a large number of statistically representative combinations of bridge parameters are generated using the LHS method, and each configuration is used to develop detailed FE models in OpenSees. These FE models are subjected to a suite of 100 representative ground motions to capture the nonlinear dynamic responses. Upon completion of all analyses, the response data, such as maximum drift ratio and abutment deformation, are extracted, organized, and prepared for the subsequent development of the PSDM and ML learning training.

ii) Using the PSDM, system-level fragility curves are developed to quantify the probability of exceeding different damage states. These fragility functions are integrated into a seismic resilience framework to evaluate key resilience metrics, including post-event functionality and recovery trajectories. Simultaneously, the PBEE framework is applied to estimate post-earthquake losses, including repair cost, time, and carbon footprint, according to the damage levels.

iii) The complete dataset, comprising key bridge attributes as input features, along with their corresponding seismic resilience and post-earthquake losses as output, is compiled. This dataset is then partitioned into 80 % for training and 20 % for testing. Several widely used ML models, such as Decision Trees, Random Forests, and Artificial Neural Networks, are trained using the training subset. To ensure robust generalization and prevent overfitting, *k*-fold cross-validation and hyperparameter tuning are performed to identify the most suitable ML model.

iv) The optimal ML model is employed as a rapid predictive tool for estimating PSDM, seismic resilience, and post-earthquake losses of regional RC bridges based on input features such as column height, column diameter, span length, concrete strength, and steel strength. Additionally, the ML-based framework facilitates feature importance and sensitivity analyses, providing valuable insights to optimize bridge design and support decision-making.

3. Regional RC bridges

To illustrate the ML-based framework, a three-span RC bridge configuration (Fig. 2) is selected for rapid assessment of seismic resilience and post-earthquake losses, based on the assumed region's typical bridge characteristics. The bridge consists of a box-girder superstructure resting on seat-type abutments, with each span supported by two circular cross-section columns arranged symmetrically with identical spans. The key bridge attributes used to represent regional variability are selected based on typical design ranges and serve as input features in the ML framework, as well as for generating statistically varied FE models. The geometric parameters include span length (SL = 10–50 m), column height (CH = 3–15 m), column diameter (CD = 1–2 m), deck width (DW = 8–20 m), bent spacing (BS = 5–11 m), longitudinal gap (LG = 0.05–0.2 m), number of bearings (NB = 2–8), and backwall depth (BD = 1.5–2.0 m). The material properties include unconfined concrete strength (UCS = 22–35 MPa), steel yield strength (SS = 300–550 MPa), longitudinal steel bar diameter (SD = 20–50 mm), and concrete cover thickness (CT = 30–70 mm).

3.1. FE modeling

Building upon the RC bridge configuration (Fig. 2), a total of 1000 FE models are developed in the OpenSees computational platform [42], using the LHS method. In these FE models, the bridge superstructure is represented by linear 3D elastic beam-column elements, while the columns are modeled as nonlinear 3D force-based beam-column elements with fiber sections [52]. For simplicity, rigid connections between the piers and superstructure are assumed to ensure deformation compatibility and force transfer, as superstructure damage is typically limited.

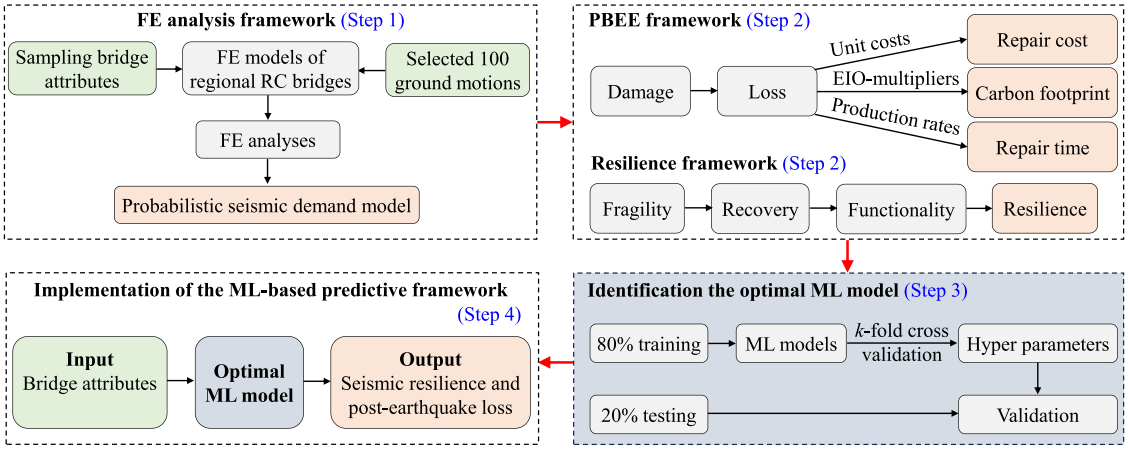

Fig. 1. ML-based framework for regional RC bridges.

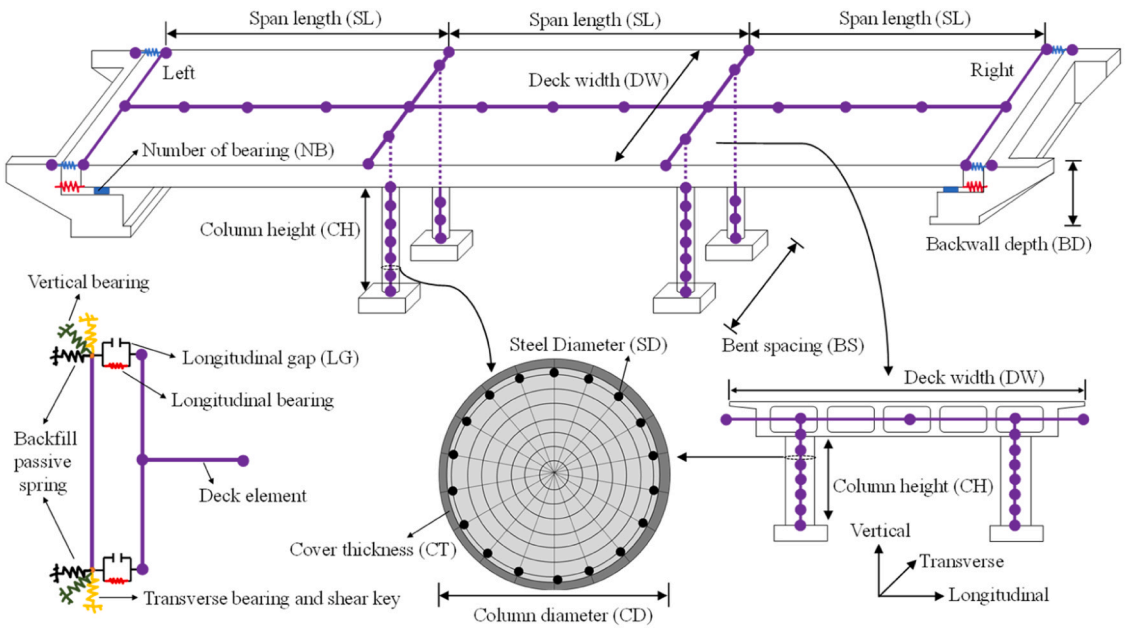

Fig. 2. Regional RC bridge configuration.

The material behavior is defined by Concrete01 material [42] to represent confined and unconfined concrete with degraded linear unloading/reloading stiffness, while the reinforcing steel rebars are modeled using the Steel02 material [42] with isotropic strain hardening.

3.2. Abutment modeling

The nonlinear behavior of seat-type abutments (Fig. 2) is simulated using a spring abutment model [6,9], implemented in OpenSees with zero-length elements representing the elastomeric bearing pads, longitudinal gap, backwall, and backfill soil. For simplicity, the abutment foundation is modeled as fixed, neglecting potential rocking or sliding effects due to soil-structure interaction, which may influence the seismic response, particularly on soft soils (e.g., [22]). In this regard, Fig. 3 shows the representative abutment response with four elastomeric bearing pads, a 5 cm gap, and a backwall (1.8 m in height and 10 m in width). From Fig. 3a, it can be seen that once the longitudinal gap closes, passive backfill pressure begins to mobilize and acts against the backwall. In the transverse direction, the abutment response is governed by the combined action of the elastomeric bearing pads, exterior concrete shear keys, wing walls, and soil backfill (Figs. 2 and 3b).

3.3. FE model validation for bridge RC column

To ensure the accuracy of the FE model, calibration is performed using experimental results from an RC bridge column test [11], which is part of the regional RC bridge configuration described in Fig. 2. The column has a diameter of 1.52 m, a height of 9 m, and 25 longitudinal rebars with a diameter of 42 mm, along with a concrete cover of 5 mm thickness. The material properties include confined concrete with a compressive strength of −34.5 MPa [11] and a crushing strength of −20.7 MPa [21], unconfined concrete with a compressive strength of −27.6 MPa [11], and reinforcing steel with a yield strength of 475 MPa and an elastic modulus of 206 GPa [21]. For the OpenSees Steel02 model, the strain hardening ratio ($b = 0.001$) and transition parameters ($R_0 = 18$, $CR_1 = 0.925$, and $CR_2 = 0.15$) are kept constant for simplicity in this study. Using these parameters, the force-displacement relationship obtained from the FE simulation is compared with the experimental data (Fig. 4). As seen in Fig. 4, the close agreement validates the accuracy of the FE model in capturing the nonlinear behavior of the RC column under cyclic loading, providing a reliable basis for further evaluating seismic performance, resilience, and post-earthquake losses of RC bridges.

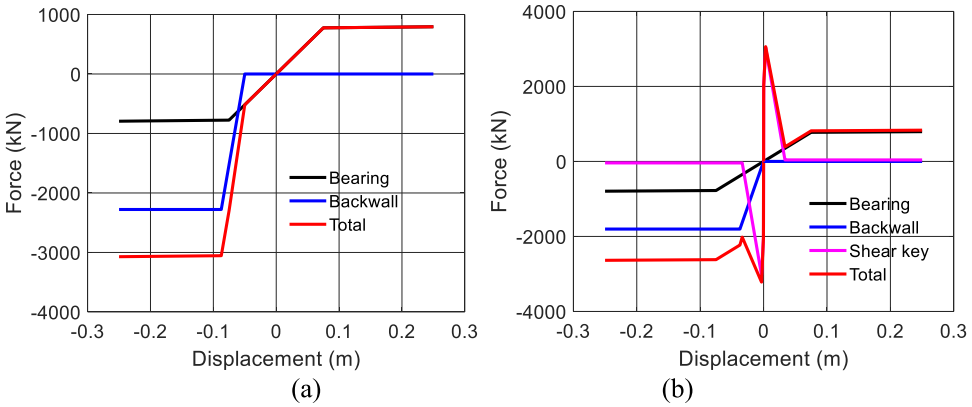

Fig. 3. Abutment model response: (a) Longitudinl; (b) Transverse.

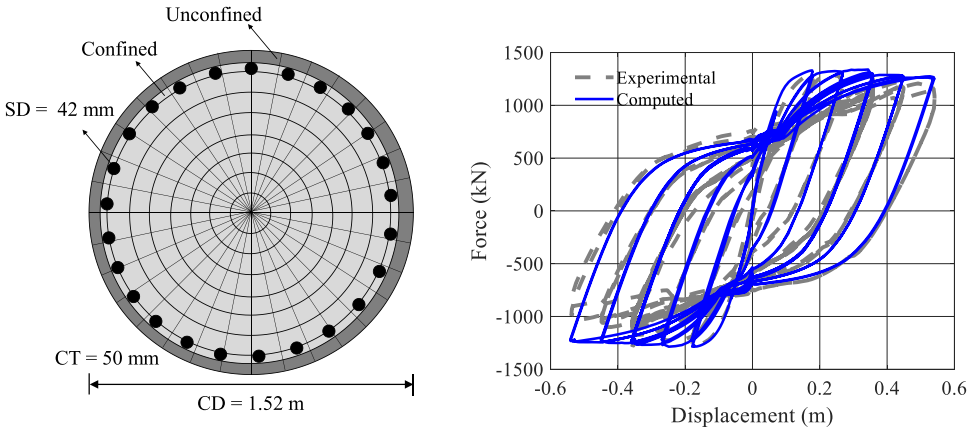

Fig. 4. Force-displacement of a representative bridge RC column.

3.4. Ground motions

A set of 100 earthquake ground motions (Fig. 5) is employed, including 20 pairs of near-fault pulse-like motions [37] and 80 pairs of far-field motions [26]. Each motion pair consists of two perpendicular horizontal acceleration time history components (i.e., longitudinal and transverse in Fig. 2), uniformly applied to both the bridge piers and abutment spring models to ensure consistent seismic excitation across all supports. The selected motions have moment magnitudes (M_w) ranging from 5.8 to 7.2 and epicentral distances (R) between 0 and 60 km, categorized into five groups (Fig. 5a): Small Magnitude Large Distance (SMLR), Small Magnitude Small Distance (SMSR), Large Magnitude Large Distance (LMLR), Large Magnitude Small Distance (LMSR), and Near-fault motions ($R < 15$ km). For illustration, Fig. 5b displays the spectral acceleration of the selected ground motions, with the median values (red line) highlighting the central tendency while capturing variations in frequency content and amplitude. Fig. 5c presents the histogram of SRSS (Square Root of the Sum of Squares) PGA values, where most motions fall below 0.5 g, with a few exceeding 1 g.

4. Performance-based earthquake engineering framework

To evaluate the post-earthquake losses of the regional RC bridges, the developed ML-based framework integrates the 3D FE models with the PBEE methodology [36,38,4,49,48] and the Economic Input-Output Life Cycle Assessment (EIO-LCA) approach [14]. Within this framework, seismic performance is characterized using six performance groups (PGs), each corresponding to a specific engineering demand parameter: PG1 and PG2 relate to maximum and residual drift of columns, PG3 and PG4 represent relative abutment displacements, and PG5 and PG6 reflect bearing displacements in the longitudinal and transverse directions, respectively. For each PG, damage is classified into discrete damage states (*DS*1 to *DS*4), facilitating a systematic assessment of repair needs for columns, abutments, and bearings based on increasing severity from slight to complete failure (Table 1). As shown in Table 1, while PG1 and PG2 may have the similar *DS* classification (e.g., *DS*1), their repair consequences differ considerably due to the different structural effects of instantaneous versus residual drift (as discussed in

Table 1
Damage states (*DS*) for each performance group (PG).

PG #	1	2	3, 4	5, 6
-	Maximum drift ratio (%)	Residual drift ratio (%)	Maximum relative longitudinal abutment displacements (m)	Maximum bearing displacement (m)
Slight *DS*1	(Cracking) $\lambda = 0.3$ $\beta_C = 0.3$	(Threshold) $\lambda = 0.50$ $\beta_C = 0.3$	(Joint cleaning) $\lambda = Gap/2$ $\beta_C = 0.25$	(Yielding) $\lambda = 0.076$ $\beta_C = 0.25$
Moderate *DS*2	(Spalling) $\lambda = 1.65$ $\beta_C = 0.33$	(Thicken pier) $\lambda = 1.25$ $\beta_C = 0.4$	(Joint seal assembly) $\lambda = Gap$ $\beta_C = 0.25$	(Failure) $\lambda = 0.152$ $\beta_C = 0.25$
Extensive *DS*3	(Bar buckling) $\lambda = 6.0$ $\beta_C = 0.25$	(Re-center) $\lambda = 2.0$ $\beta_C = 0.4$	(Backwall spalling) $\lambda = Gap/2 + 0.5\ \%$ × abutment depth $\beta_C = 0.3$	N/A
Complete *DS*4	(Failure) $\lambda = 6.7$ $\beta_C = 0.35$	(Failure) $\lambda = 6.7$ $\beta_C = 0.35$	(Backwall spalling) $\lambda = Gap/2 + 2\ \%$ × abutment depth $\beta_C = 0.3$	N/A

λ represents the median value, and β_C denotes the logarithmic standard deviation.

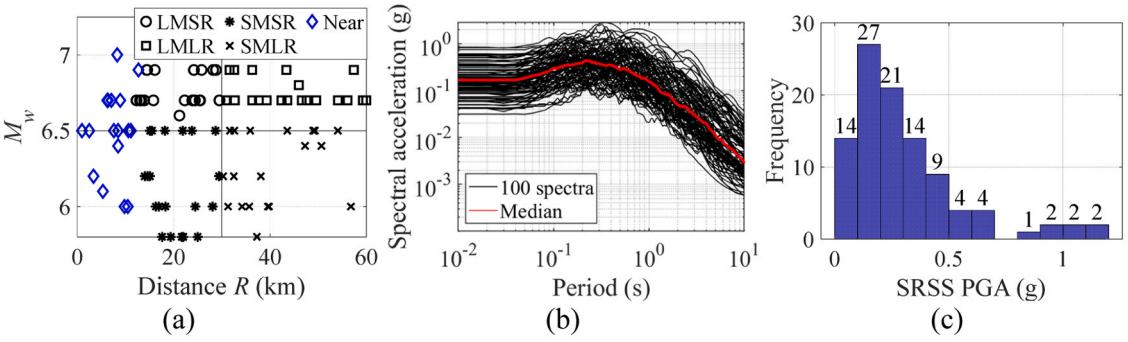

Fig. 5. Based input motions: (a) Distribution; (b) Spectral acceleration; (c) Histogram.

[38]). Specifically, PG1 at *DS*1 involves minor surface repairs such as epoxy injection, whereas PG2 at *DS*1 may require more extensive interventions, including steel casing, reinforcement replacement, and backfilling, due to permanent deformation [38]. Moreover, it is noted that *DS*3 (bar buckling, 6 %) and *DS*4 (failure, 6.7 %) in PG1 are triggered at the same drift thresholds without accounting for variations in concrete cover, confinement, or other section-level properties.

4.1. Probabilistic seismic demand model

The PSDM [16] establishes a relationship between the seismic demand (S_D) of performance groups (Table 1) and the intensity measure (IM) of selected ground motions. Typically, the S_D is modeled as a two-parameter lognormal distribution, with its median expressed using a power-law equation [16,36,38]:

$$S_D = a \cdot IM^b \tag{1}$$

where, a and b are the power-law model parameters, determined through linear regression in logarithmic space as:

$$\ln(S_D) = \ln(a) + b \cdot \ln(\mathrm{IM}) \tag{2}$$

Fig. 6 illustrates the violin plots for the distribution of power-law model parameters a and b across 1000 bridges subjected to 100 ground motions for six PGs (Table 1). For parameter a (i.e., the intercept in Eq. 2), PG1 exhibits the highest median values and the widest distribution, indicating that seismic demand can be substantial even at low shaking intensities, accompanied by higher variability. For parameter b (i.e., the slope in Eq. 2), PG2 (Table 1) exhibits higher median values and greater variability, indicating that the residual drift ratio is more sensitive to increases in ground motion intensity. In contrast, PG3, PG4 (maximum relative longitudinal abutment displacements) and PG5, PG6 (maximum bearing displacements) show lower b values with narrower distributions, suggesting weaker sensitivity to seismic intensity.

4.2. Loss model

The loss model [36,38] relates repair quantities (Q) to specific damage states (*DS*) through a piecewise linear relationship:

$$Q = e_{lin} \cdot DS + f_{lin} \tag{3}$$

where $e_{lin} = \Delta Q / \Delta DS$ and $f_{lin} = Q - e_{lin} \Delta Q / \Delta DS$ represent the slope and intercept in linear space, respectively. To align with the PSDM, the loss model also adopts a log-linear relationship between DS and Q in logarithmic space:

$$\ln(Q) = E + F \cdot \ln(DS) \tag{4}$$

where E and F [36,38,4,49] are coefficients relating Q and *DS* in a logarithmic space, derived from the first-order Taylor series expansion of $\ln(Q) = \ln(e_{lin} \cdot DS + f_{lin})$ around the median PSDM value $d_0 = e^{a+b \cdot \ln(\mathrm{IM})}$). Consequently, the total repair quantities (Q) for a specific repair item (Table 2), encompassing all PGs (Table 1), can be feasibly estimated, given an IM and its corresponding median PSDM value.

Table 2
Production rate, unit cost, and emission factor for each repair item.

Repair item #	Production rate (CWD)	Unit cost (Dollar $)	Emission factor (t CO_2/million $)
1. Excavation of structure	1.2	216/m^3	457.1
2. Backfilling of structure	2.2	288/m^3	457.1
3. Temporary superstructure support	34.2	409/m^2	1000
4. Temporary abutment support	33.2	409/m^2	1000
5. Structural concrete for bridge	10.0	2910/m^3	333.33
6. Structural concrete for approach slab	2.0	2124/m^3	3285.7
7. Reinforcing steel for bridge	1.8	3.0/kg	4000
8. Epoxy injection for crack repair	2.0	705/m	2500
9. Repair minor spalls	2.0	3226/m^2	1000
10. Steel casing for columns	70.0	22/kg	1000
11. Joint seal assembly	2.0	902/m	2000
12. Elastomeric bearings	1.2	1500/EA	2500
13. Bridge removal	2.0	3078/m^3	500
14. Approach slab removal	4.0	1307/m^3	562.5

4.3. Post-earthquake losses

The post-earthquake repair cost $E[C_i]$ is calculated by multiplying the unit cost UC_i (Table 2) with the expected repair quantity $E[Q_i]$ derived from Eq. (4). As such, the total expected repair cost is obtained by summing the contributions of all repair items ($NQ = 14$ in Table 2):

$$E[C] = \sum_{i=1}^{NQ} E[C_i] = \sum_{i=1}^{NQ} UC_i \bullet E[Q_i] \tag{5}$$

The carbon footprint of the post-earthquake repair process is obtained using the EIO-LCA methodology [14,36,38,4,49,48], accounting for emissions across the entire supply chain and expressed as:

$$E[Carbon] = \sum_{i=1}^{NQ} E[EF_i] E[C_i] \tag{6}$$

where $E[EF_i]$ represents the emission factors (t CO_2/$) for each repair item (Table 2, [38,57,36]). Additionally, the post-earthquake repair time is quantified as the total crew working days (CWD) for project completion, calculated using the following equation [36,38]:

$$E[RT] = \sum_{i=1}^{N_Q} PR_i \tag{7}$$

where PR_i represents the production rate for each repair item (Table 2), assumed to be constant and independent of the expected repair quantities $E[Q_i]$. Repair activities are initiated only if $P(E[Q_i] \geq tol) > 0.5$, where the tolerance set at 3 % of the maximum expected repair quantity.

Fig. 7 illustrates the post-earthquake losses, including repair cost, carbon footprint, and repair time for all bridge models, with mean trends (red line) and variability represented by the 5th and 95th percentile bounds (blue dashed lines). As shown, both repair cost and carbon

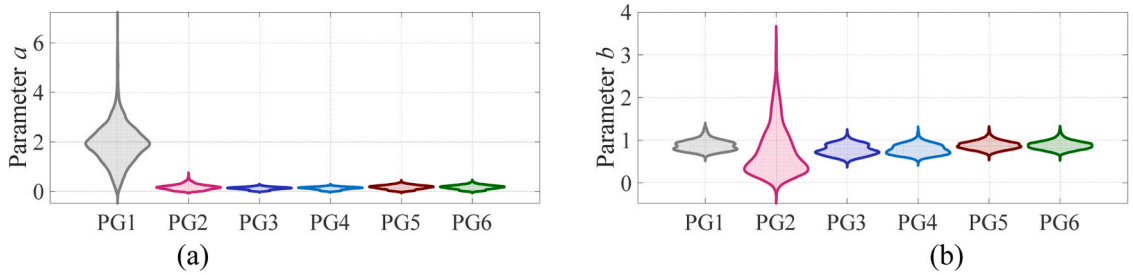

Fig. 6. Power-law model parameters: (a) Parameter a; (b) Parameter b.

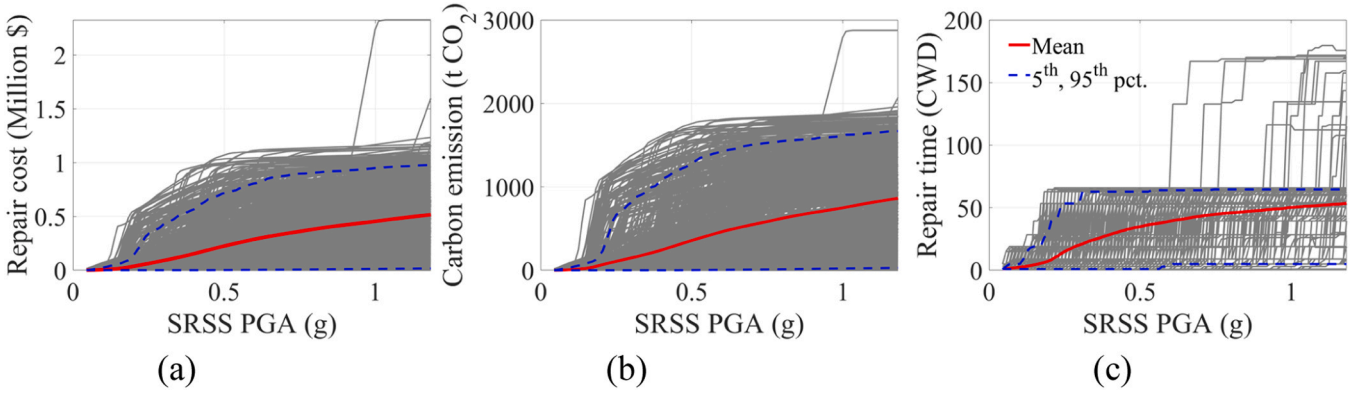

Fig. 7. Post-earthquake losses: (a) Repair cost; (b) Carbon footprint; (c) Repair time.

emission rise significantly as SRSS PGA increases, reflecting greater damage severity and the resulting higher repair efforts. Similarly, repair time (Fig. 7c) increases at higher SRSS PGA levels, highlighting the extended efforts required for recovery under severe seismic conditions.

5. Seismic resilience framework

Seismic resilience (Fig. 8) is defined as the ability of a structure to withstand seismic events, recover from damage, and maintain or restore functionality over time [13,18,8]. Drawing upon these foundational studies, this section presents a comprehensive overview of the seismic resilience framework for RC bridges under earthquakes, emphasizing the integration of system-level fragility and time-dependent recovery models. While the underlying models are derived from the established frameworks [13,18,8], they are employed here to ensure methodological consistency and to enable seamless integration with the ML-based predictive component.

5.1. Seismic fragility model

Component seismic fragility [45,50,60] quantifies the probability $P(S_D \geq S_C|\text{IM})$ that the S_D (Eq. 1) of a bridge component (i.e., PGs in Table 1), where S_C represents the structural capacity (or λ in Table 1) at a given level of IM:

$$P(S_D \geq S_C|\text{IM}) = \Phi\left[\frac{\ln(S_D) - \ln(S_C)}{\sqrt{\beta_{D/\text{IM}}^2 + \beta_C^2}}\right] \tag{8}$$

where $\Phi[\ ]$denotes the cumulative standard normal distribution function, $\beta_C$represents the dispersion of the predefined damage states (Table 1), and $\beta_{D/\text{IM}}$ is the dispersion of the S_D conditioned on a specific IM, given by:

$$\beta_{D/\text{IM}} = \sqrt{\frac{\sum_{i=1}^{N}[\ln(d_i) - \ln(S_D)]^2}{N-2}} \tag{9}$$

where $N = 100$ represents the total number of nonlinear dynamic FE analyses conducted for each sampling model, and d_i denotes the i^{th} FE result.

System-level fragility [45] quantifies the probability of a structural system exceeding a given damage state under a specific IM by aggregating component fragilities, capturing both upper and lower bounds of system behavior. The upper bound represents the conservative scenario, where the bridge system is assumed to fail if any component fails (i.e., a series system), and is calculated as the maximum of individual component fragilities:

$$P_{upper} = \max\{P_1, P_2, \ldots P_n\} \tag{10}$$

Conversely, the lower bound represents the optimistic scenario, in which the system is assumed to fail only when all components fail (i.e., a parallel system), and is calculated using joint probability that all components survive:

$$P_{lower} = 1 - \prod_{i=1}^{n}(1 - P_i) \tag{11}$$

In Eqs. (10) and (11), P_i is the fragility of the i^{th} component, and n denotes the number of bridge components (i.e., PG1-PG6 in Table 1). To estimate a representative system-level fragility, this study adopts the average of the upper and lower bounds, $P_{Average} = (P_{Upper} + P_{Lower})/2$.

5.2. Recovery model

A recovery model (Fig. 8) evaluates the time-dependent process of restoring functionality from a damaged state back to its original or near-original condition [18]:

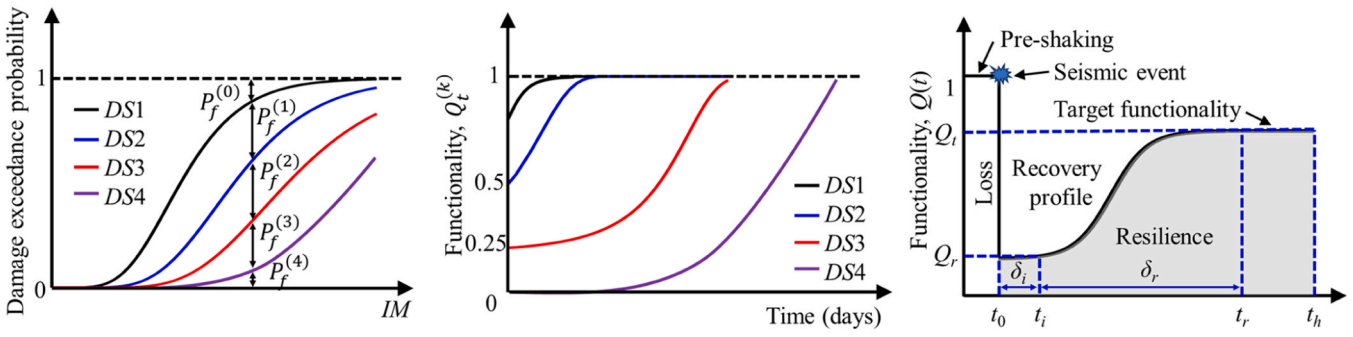

Fig. 8. Seismic resilience framework.

$$Q(t|IM) = P^0(\mathrm{IM})\cdot 1 + \sum_{k=1}^{3} P^k(\mathrm{IM})\cdot Q^{(k)}(t) \tag{12}$$

where $P^0(\mathrm{IM})$ represents the fragility of the bridge system remaining undamaged after the earthquake, and $P^k(\mathrm{IM})$ denotes the fragility of being in the k^{th} damage state. To ensure consistency with the established resilience assessment framework and to provide a structured methodology to quantify time-dependent recovery for varying damage states (Table 1), this study adopts three representative recovery functions, including rapid, gradual, and delayed restoration trajectories [18,25,65,7].

$$R_f^n = 1 - e^{-\omega\eta} \tag{13}$$

$$R_f^s = \frac{1-\cos(\pi\eta)}{2} \tag{14}$$

$$R_f^p = e^{-\omega(1-\eta)} \tag{15}$$

where $\omega = 10$ represents the shape parameter controlling the rate of recovery [65,7], $\eta = (t - t_i)/\delta_r$ is a normalized time variable ranging from 0 to 1, t_i is the start time of the recovery process and δ_r is the total recovery duration (Fig. 8). In Eqs. (13–15), the functions R_f^n (negative exponential), R_f^s (sinusoidal), and R_f^p (positive exponential), represent the rapid (*DS*1), gradual (*DS*2), and delayed (*DS*3, *DS*4) recovery processes, respectively, corresponding to increasing damage severity as defined in Table 1.

5.3. Seismic resilience

Seismic resilience [18,28,48,47,65,7,8] is obtained by integrating the recovery model (Eq. 12) over the specified time horizon, as follows:

$$Resilience = \frac{1}{t_h - t_0}\int_{t_0}^{t_h} Q(t)dt \tag{16}$$

where t_0 denotes the time of the earthquake event occurrence, and t_h refers to the time horizon investigated after the recovery process. When an earthquake occurs (Fig. 8), the functionality $Q(t)$ of the bridge system drops to a residual level Q_r and can be recovered through restoration activities (Table 2) conducted during the specified recovery period $\delta_r = t_r - t_i$, where $t_i = t_0 + \delta_i$ denotes the initial time of the restoration process, and δ_i (taken as 1 day) indicates the idle time. For simplicity, the recovery period δ_r is assumed to be the repair time (Eq. 7) in this study.

Fig. 9 illustrates the system-level fragility at *DS*1-*DS*4 and seismic resilience with mean trends (red line) and variability represented by the 5th and 95th percentile bounds (blue dashed lines). It can be seen that as the SRSS PGA increases, the system-level fragility rises at all damage levels (i.e., *DS*1-*DS*4), reflecting a higher probability of failure under more intense seismic shaking (Fig. 9a-d). In contrast, seismic resilience (Fig. 9e) decreases with the SRSS PGA levels, with high resilience observed at lower PGAs due to minimal damage and rapid recovery, while more intense ground motions result in sharp reductions in seismic resilience, illustrating the challenges of maintaining functionality under extreme earthquake events.

6. Machine learning-based framework

Six commonly used ML models are employed in this study, including Decision Tree (DT), Artificial Neural Network (ANN), Support Vector Machine (SVM), Random Forest (RF), Gradient Boosting Decision Tree (GBDT), and K-Nearest Neighbors (KNN). These models are selected for their ability to address both linear and non-linear relationships and their effectiveness in handling regression and classification problems. For instance, DT provides interpretability and reduces overfitting through pruning, ANN captures complex non-linear interactions, SVM applies kernel functions to model non-linear relationships, KNN identifies localized local trends, and ensemble methods such as RF and GBDT offer robust and accurate predictions.

6.1. Hyperparameters tuning

To optimize performance and avoid overfitting, hyperparameters of each model are fine-tuned using grid search combined with five-fold cross-validation. The key bridge attributes serve as input parameters, with seismic resilience values (from 1000 models under 100 motions) as the output for simplicity. Subsequently, the dataset is split into 80 % for training and 20 % for testing to train and validate the ML models (Fig. 1). During cross-validation, the training data is split into five subsets, with four used for training and one for validation in each iteration. This process is repeated five times, and the average accuracy across all iterations is used to identify the optimal hyperparameters for each ML model.

Fig. 10 illustrates the influence of key hyperparameters on the accuracy of six ML models for seismic resilience prediction, with accuracy trends depicted as lines and shaded regions representing uncertainty bounds. For ANN (Fig. 10a), accuracy improves as the number of neurons increases, reaching optimal performance at 20 neurons, while a lower learning rate (e.g., 0.001) effectively reduces variability. RF (Fig. 10b) achieves high accuracy with 10 estimators, with deeper trees (e.g., 10 levels) slightly enhancing accuracy but increasing variability. For KNN (Fig. 10c), optimal accuracy is observed with 2 neighbors, where the Euclidean metric consistently outperforms others across the tested range, supporting its selection as the most suitable option. GBDT (Fig. 10d) performs optimally with 300 estimators and a high learning rate (e.g., 0.1), effectively minimizing variability. SVM (Fig. 10e) shows strong performance at $\gamma = 0.1$, while DT (Fig. 10 f) maintains consistent

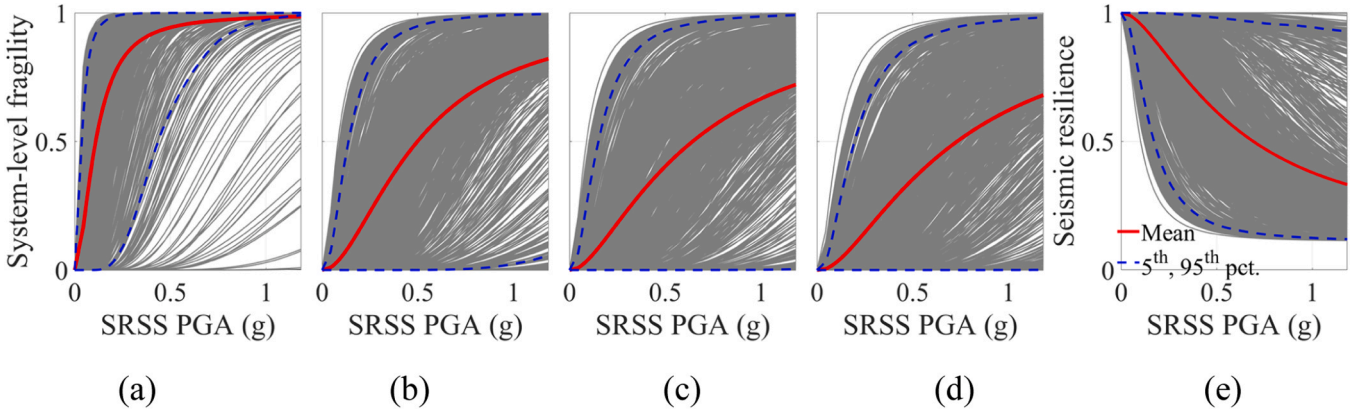

Fig. 9. Overall resuts: (a)-(d) System-level fragility at *DS*1-*DS*4; (e) Seismic resilience.

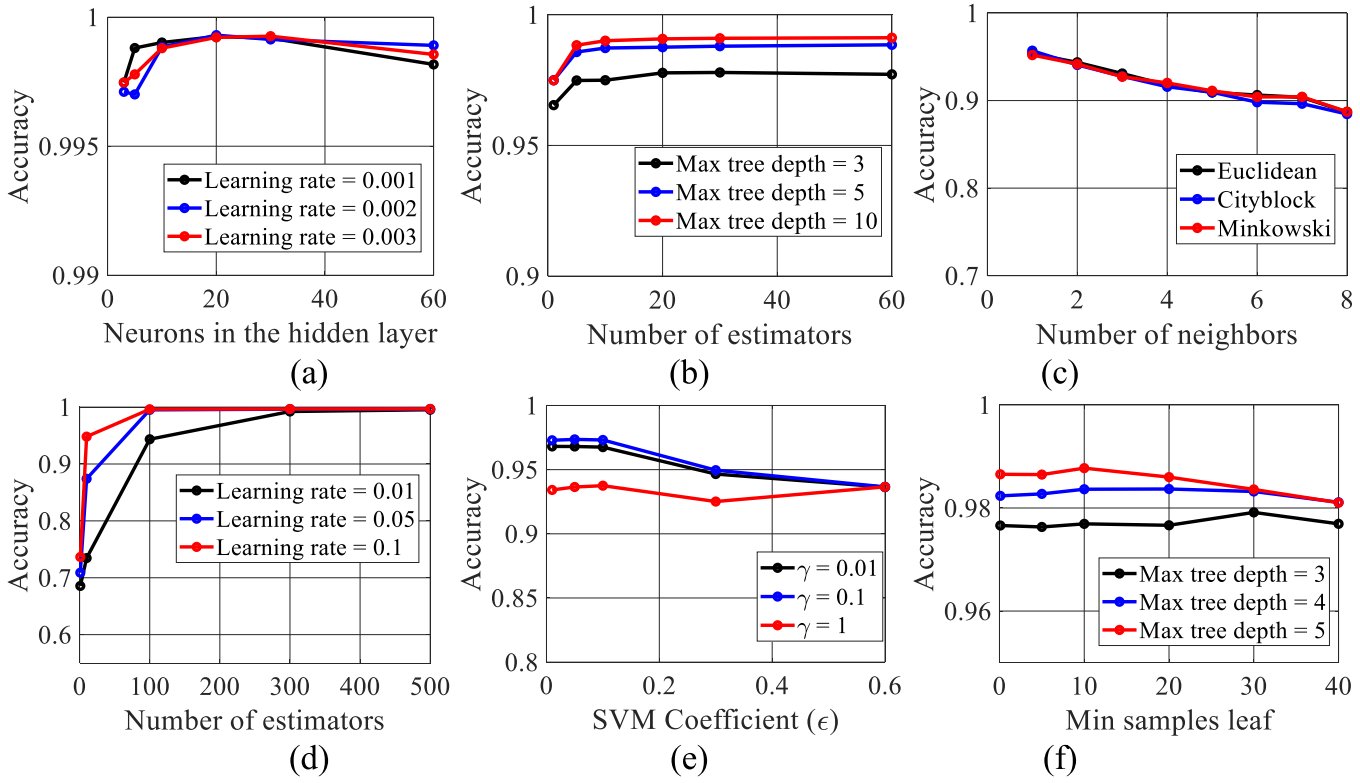

Fig. 10. Influences of hyperparameters on the ML model performance: (a) ANN; (b) RF; (c) KNN; (d) GBDT; (e) SVM; (f) DT.

accuracy at tree depths of 5 with smaller leaf sizes (e.g., 5).

6.2. ML model performance evaluation

Fig. 11 evaluates the performance of ML models for predicting seismic resilience under varying SRSS PGA levels (0.3 g, 0.6 g, 0.9 g, and 1.2 g), using root mean square error (RMSE), mean absolute error (MAE), and the coefficient of determination (R^2). It can be observed that the ANN consistently outperforms the other models, achieving the highest R^2 values (above 0.94) and the lowest RMSE and MAE across all

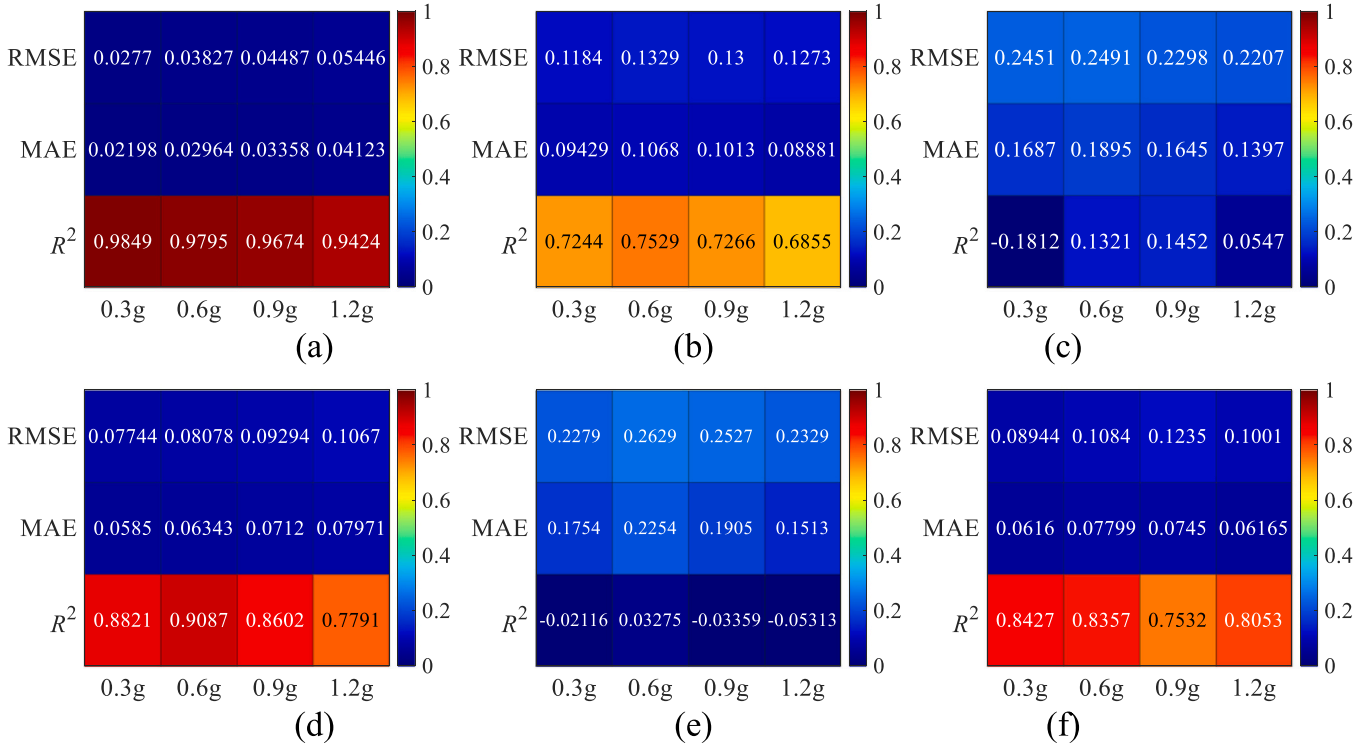

Fig. 11. Model performance (RMSE, MAE, and R^2) in predicting seismic resilience: (a) ANN; (b) RF; (c) KNN; (d) GBDT; (e) SVM; (f) DT.

SRSS PGA levels, demonstrating its ability to capture complex non-linear relationships. GBDT also performs well, with R^2 values between 0.77 and 0.91 and relatively low prediction errors. RF shows moderate performance, with R^2 values peaking at 0.75 but declining at extreme SRSS PGAs. DT provides moderate accuracy at specific SRSS PGA levels but lacks consistency, as its performance fluctuates across different intensity levels. In contrast, KNN and SVM underperform significantly, with poor R^2 values and high errors, highlighting their limitations for this application. Overall, ANN stands out as the most reliable model and is implemented as the predictive framework for the subsequent rapid seismic resilience and sustainability assessment of regional RC bridges.

6.3. Feature relative importance

To assess the contribution of individual bridge attributes to seismic resilience predictions, feature importance is evaluated by systematically permuting each attribute and measuring its impact on model performance (R^2). While similar trends can also be observed using the MAE or MSE, R^2 is adopted in this section due to its intuitive interpretability as a proportion of variance explained. After permutation, the drop in R^2 is calculated and normalized by the total sum of all absolute R^2 reductions to determine each feature's relative importance. For illustration, Fig. 12 presents the relative importance of various attributes for predicting seismic resilience using the ANN model across different SRSS PGA levels (i.e., 0.3 g, 0.6 g, 0.9 g, and 1.2 g).

i) At low shaking levels (0.3 g), the longitudinal gap is the most critical feature due to gap closure (Fig. 12a), strongly affecting seismic resilience predictions. Column height and span length have moderate influence but do not significantly impact resilience under low-intensity shaking.
ii) As shaking intensity increases (0.6 g and above), column height becomes dominant (Fig. 12b-c), reflecting its role in structural performance under severe conditions. Generally, taller columns are more susceptible to lateral forces, thus reducing resilience. While longitudinal gap and span length remain relevant, their influence diminishes relative to column height.
iii) At the highest intensity (1.2 g), deck width and column diameter show slightly increased importance due to their role in nonlinear behavior, though column height and span length remain the most influential attributes.

7. Rapid resilience and PBEE assessment of RC bridges

After developing and optimizing the ML model using the ANN, it is implemented as a predictive tool to rapidly predict seismic demand, system-level fragility, seismic resilience, and post-earthquake losses for regional RC bridges. As an illustrative application, three hypothetical RC bridges (#1, #2, and #3 in Fig. 13 and Table 3), each with distinct attributes, are assumed for the purpose of this study to demonstrate the capabilities of the ML-based framework. The key parameters of these bridges, including span length, column height, column diameter, and other critical attributes listed in Table 3, are employed as input variables for the ANN model.

7.1. Predicted seismic demand

Fig. 14 presents the predicted seismic demand (i.e., PG1-PG6) for three representative regional RC bridges (Bridge #1–3) across various SRSS PGA levels. The equations (obtained from Eq. 2) shown in each plot represent the linear regression fits in log space, demonstrating the change in seismic demand (i.e., PG1-PG6) with increasing SRSS PGA for each bridge. In general, all bridges exhibit a higher seismic demand as ground motion intensity rises, highlighting the expected increase in structural response under stronger seismic conditions.

7.2. Predicted repair quantities

For further illustration, Fig. 15a presents the relationship between repair quantities (RQ3, RQ5, RQ7, and RQ9 in Table 2) and PG1 (maximum drift ratio in Table 1) for the representative RC bridges. It can be observed that the repair quantities rise as PG1 increases, indicating that higher drift ratios correspond to more severe damage and greater repair needs. For RQ3 (temporary superstructure support), RQ5 (structural concrete), and RQ7 (reinforcing steel), the repair quantities increase significantly when the drift ratio reaches 6.0 % (corresponding to DS3, bar buckling) and remain constant at higher drift ratios (above 6.7 %, DS4, failure), demonstrating that extensive repairs or replacements are needed once DS4 is triggered. For RQ9 (repair minor spalls), the repair quantities initially increase with drift ratios but decrease to zero when the drift exceeds 6.0 %. This indicates that minor repairs are no longer sufficient beyond this threshold, and full replacement is required if the drift reaches 6.7 % (Table 1).

Fig. 15b shows the repair quantities (RQ1, RQ3, RQ7, and RQ13) in relation to PG3, which represents the maximum relative longitudinal abutment displacements. As PG3 increases, the repair quantities increase significantly, indicating more severe damage and a greater need for repairs. For RQ1 (excavation of structure), RQ3 (temporary superstructure support), RQ7 (reinforcing steel), and RQ13 (bridge removal), the repair quantities remain relatively low until the abutment displacement exceeds DS1. Once this threshold is exceeded, the repair quantities rise sharply. Specifically, for Bridge #1 and #2, repair quantities remain low at lower PG3 values, but once the abutment displacement exceeds DS1, the repair quantities increase significantly. For Bridge #3, repair quantities increase more rapidly and at smaller displacements due to its smallest longitudinal gap (10 cm), which causes

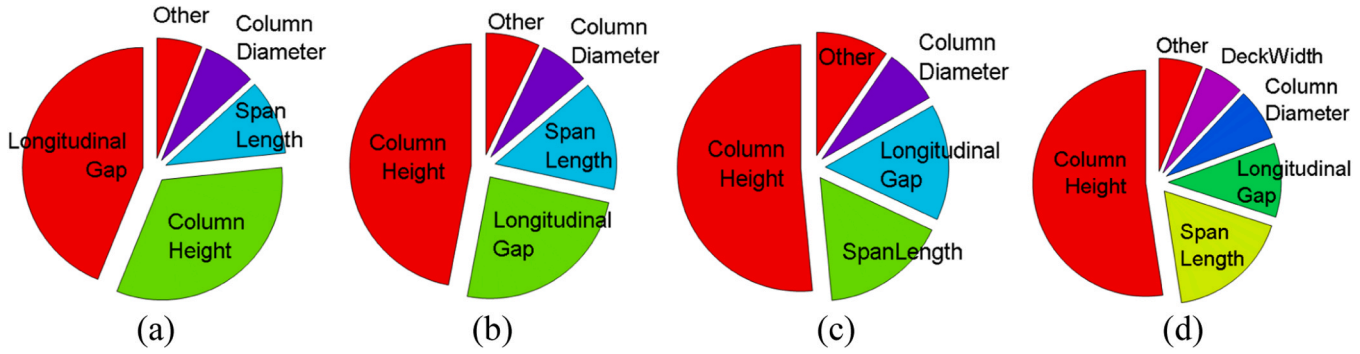

Fig. 12. Relative importance by R^2: (a) 0.3 g; (b) 0.6 g; (c) 0.9 g; (d) 1.2 g.

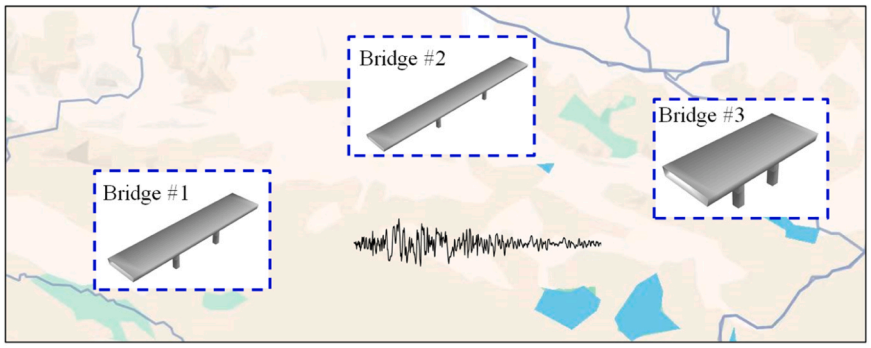

Fig. 13. Representative regional RC bridges.

Table 3
Attributes of representative regional RC bridges.

Attributes	SL (m)	CH (m)	CD (m)	CT (mm)	UCS (MPa)	SS (MPa)	SD (mm)	BS (mm)	LG (m)	NB (-)	DW (m)	BD (m)
Bridge #1	27	8	1.2	0.05	31.6	425	0.036	6	0.12	8	10	1.6
Bridge #2	40	9	1.6	0.07	35.2	525	0.045	7	0.15	8	12	1.8
Bridge #3	20	12	1.2	0.05	32.5	475	0.03	9	0.10	10	16	10

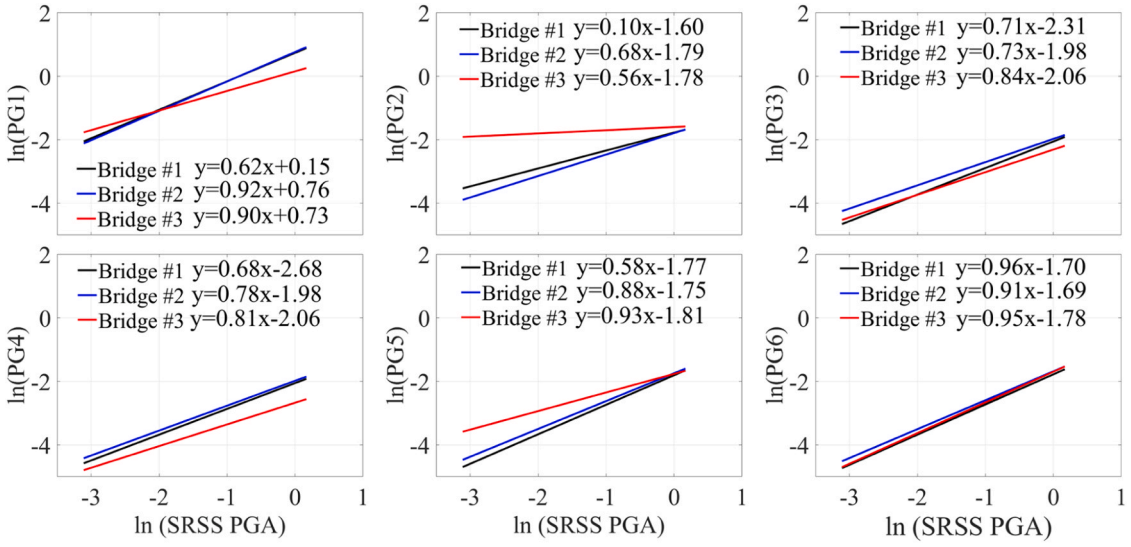

Fig. 14. PSDM of PGs for Bridges #1–3.

damage states to trigger earlier than in the other bridges.

7.3. Predicted system-level seismic fragility

Fig. 16 presents the predicted system-level fragility curves for the representative RC bridges at slight, moderate, extensive, and complete damage states. As SRSS PGA increases, the probability of exceeding each damage state rises, with slight damage occurring at lower PGA values and complete failure emerging at higher PGA values. For all RC bridges, the probability of slight damage increases rapidly and reaches 1 at about 0.5 g. Moderate and extensive damage states follow shortly after, with probabilities increasing significantly at SRSS PGA values around 0.7 g. Complete failure becomes more pronounced at higher PGAs, but Bridge #3 consistently exhibits a lower probability of failure compared to Bridge #1 and Bridge #2, demonstrating its greater resilience and ability to withstand higher levels of seismic intensity. While Bridge #3 has the smallest longitudinal gap (identified as the most critical feature at low PGA levels in Fig. 12), its comparatively lower overall fragility is attributed to the combined influence of other structural attributes (Table 3), such as a shorter span length and a greater number of bearings, which collectively reduce its seismic vulnerability.

7.4. Predicted recovery curves

Fig. 17 illustrates the predicted recovery curves for the representative RC bridges under varying SRSS PGA levels of 0.3, 0.6, 0.9, and 1.2 g. Due to less severe initial damage, Bridge #3 exhibits better functionality recovery (i.e., higher residual functionality and faster recovery curves) compared to Bridge #1 and Bridge #2. In contrast, Bridge #1 and 2 have more extensive damage, requiring more efforts for recovery. Despite these differences, all three bridges exhibit a similar recovery pattern, with an initial rapid improvement in functionality followed by a gradual recovery phase (Fig. 17). Additionally, the observed variations in recovery rates align closely with the levels of damage and repair needs

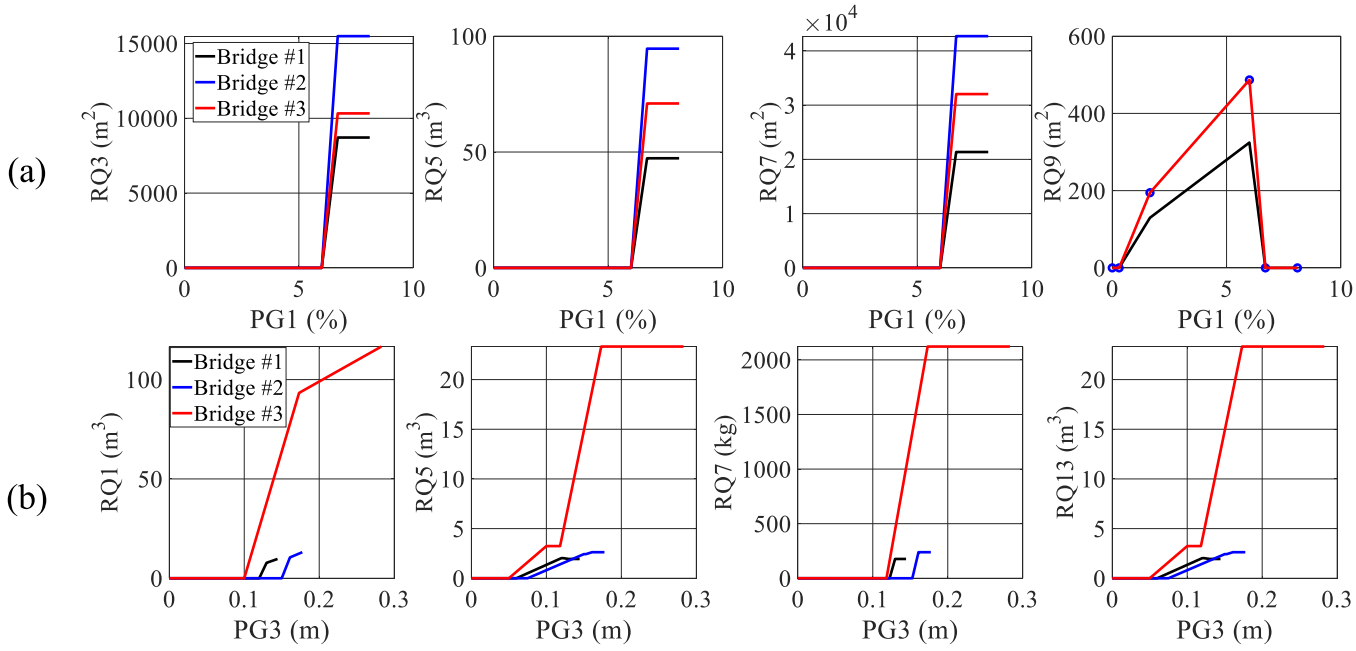

Fig. 15. Predicted repair quantities (a): PG1; (b) PG3.

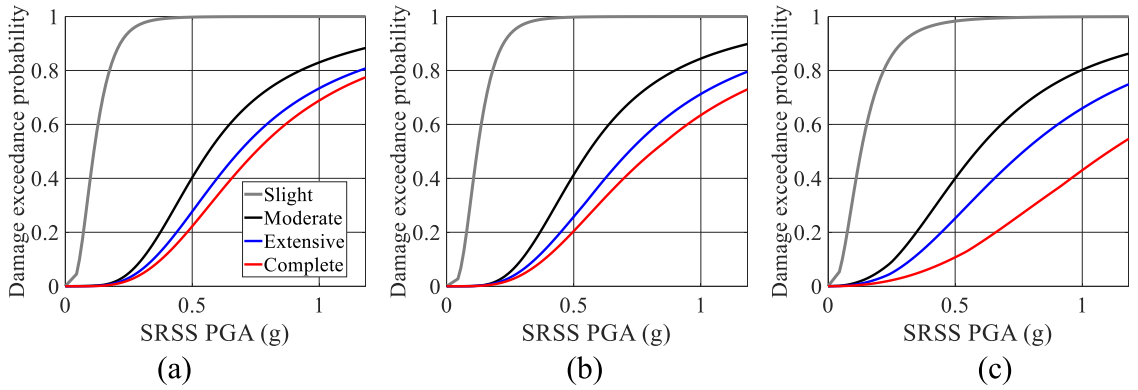

Fig. 16. Predicted system-level fragility curves: (a) Brige #1; (b) Brige #2; (c) Brige #3.

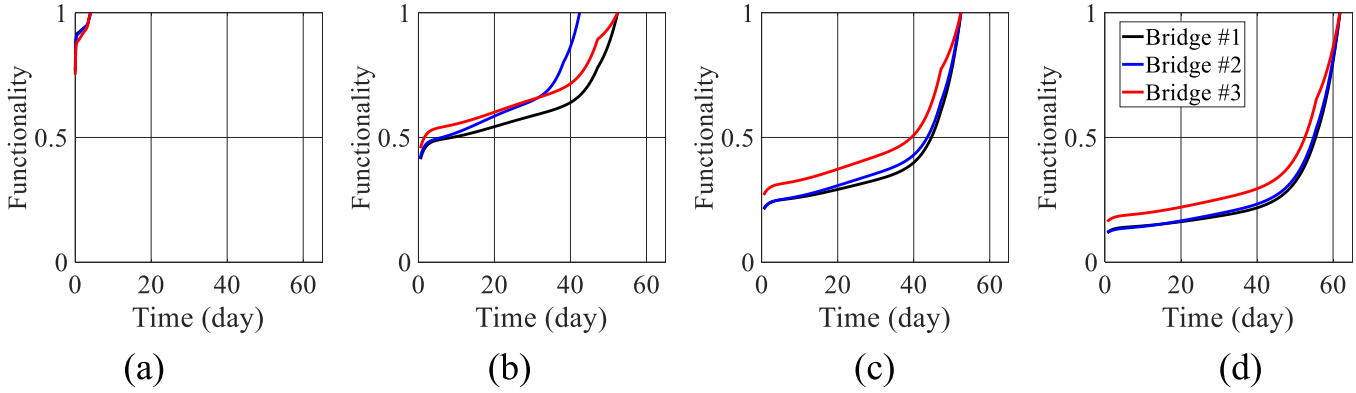

Fig. 17. Predicted recovery curves: (a) 0.3 g; (b) 0.6 g; (c) 0.9 g; (d) 1.2 g.

illustrated in the earlier fragility analysis (Fig. 14).

7.5. *Predicted seismic resilience and post-earthquake losses*

Fig. 18 presents the predicted resilience and post-earthquake losses for the representative RC bridges. As SRSS PGA increases, repair costs rise sharply, with Bridge #1 incurring the highest and Bridge #3 the lowest, reflecting more severe damage and extensive repairs for Bridge #1 (Fig. 18a). This trend also appears in carbon emissions (Fig. 18b), where Bridge #1 shows the highest values due to larger repair demands,

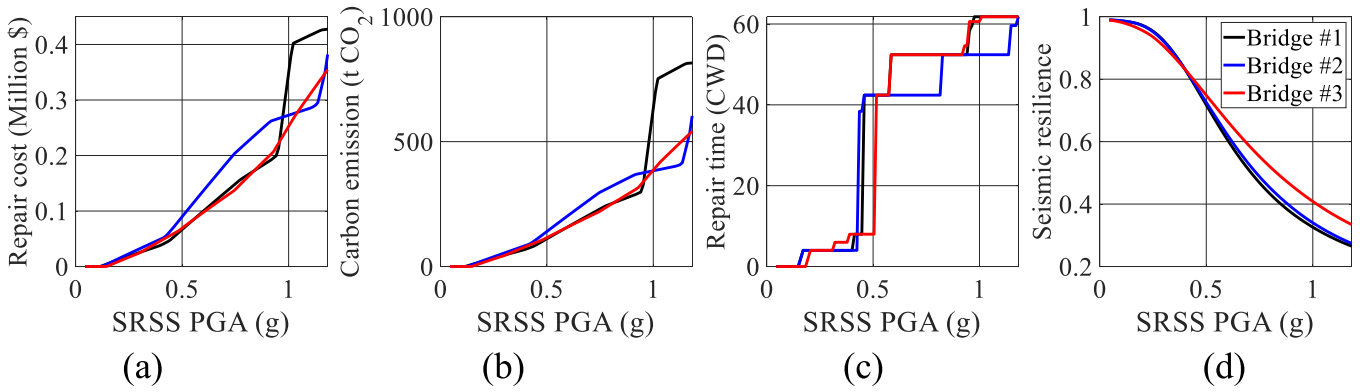

Fig. 18. Predicted results: (a) Repair cost; (b) Emission; (c) Repair time; (d) Sesmic resilience.

while Bridge #3 has lower emissions, indicating less damage and faster recovery. Additionally, seismic resilience decreases significantly with increasing PGA for all bridges (Fig. 18d), with Bridge #3 consistently showing the highest resilience, consistent with its lower fragility and shorter recovery times (Figs. 16 and 17).

Fig. 19 show the disaggregation of repair costs and carbon emissions by PGs and repair quantities (Table 2) at the highest SRSS PGA of 1.26 g. Different bridge configurations result in varying distributions of repair costs and carbon emissions across PGs and repair quantities. Specifically, Bridge #1 exhibits the highest carbon emissions for PG3 and PG4, while Bridge #3 incurs the highest repair costs for PG1 and PG4. When disaggregated by repair quantities, Bridge #1 exhibits the highest carbon emissions for RQ6 (structural concrete), while Bridge #2 incurs the highest repair costs for RQ4 (temporary support). Additionally, Bridge #1 has the highest costs in RQ4 (temporary support) and RQ6 (structural concrete), while it shows the highest carbon emissions in PG6 (structural concrete). As such, based on the disaggregated analysis of repair quantities and their associated impacts, it is evident that different repair activities contribute variably to overall costs and carbon emissions, depending on the bridge configuration and the specific type of damage sustained. This highlights the need for tailored repair and retrofit strategies that consider the unique attributes and damage scenarios of each bridge to minimize costs and environmental impacts, ultimately improving the sustainability and resilience of bridge infrastructure under seismic events.

8. Discussion

While this study incorporates a limited set of twelve key bridge attributes, it provides a computationally efficient and practical tool for the rapid assessment of seismic resilience and post-earthquake losses across regional RC bridge inventories. However, the framework does not explicitly simulate local failure mechanisms such as rebar buckling or girder unseating, and assumes simplified connection conditions between structural components. Furthermore, damage state thresholds are uniformly applied across all models without accounting for section-level variability, such as differences in concrete cover or confinement.

To further improve the fidelity and robustness of the ML framework, future studies will be conducted to: (i) incorporate reinforcement layout parameters, including tie bar spacing and stirrup configuration; (ii) extend the FE modeling to capture a broader range of potential failure modes, such as superstructure damage (e.g., deck cracking, girder unseating), foundation failure, local reinforcement instability, and the interaction between piers and the superstructure; (iii) adopt advanced feature interpretation techniques, such as SHAP (SHapley Additive exPlanations) values or conditional permutation importance, to better account for interdependencies among key input variables; (iv) validate the framework's predictions against experimental results, and observed field data; (v) expand the input parameter space to include additional geometric or material variability (e.g., number of spans, or aging-related degradation); and (vi) extend the framework to account for multi-hazard scenarios, such as combined seismic and hydrological risks, for a more comprehensive resilience assessment.

9. Summary and conclusions

This paper presents a framework that integrates the PBEE principles with ML models to enable the rapid assessment of seismic resilience and post-earthquake losses for regional RC bridges. By incorporating twelve key bridge attributes, the framework systematically develops 1000 FE bridge models using the LHS method, facilitating the computation of probabilistic seismic demand models, system-level fragility, seismic resilience, and post-earthquake losses, including repair time, repair costs, and carbon footprint. Consequently, the developed framework is applied to three representative regional RC bridges, delivering rapid and reliable predictions of seismic resilience and post-earthquake losses

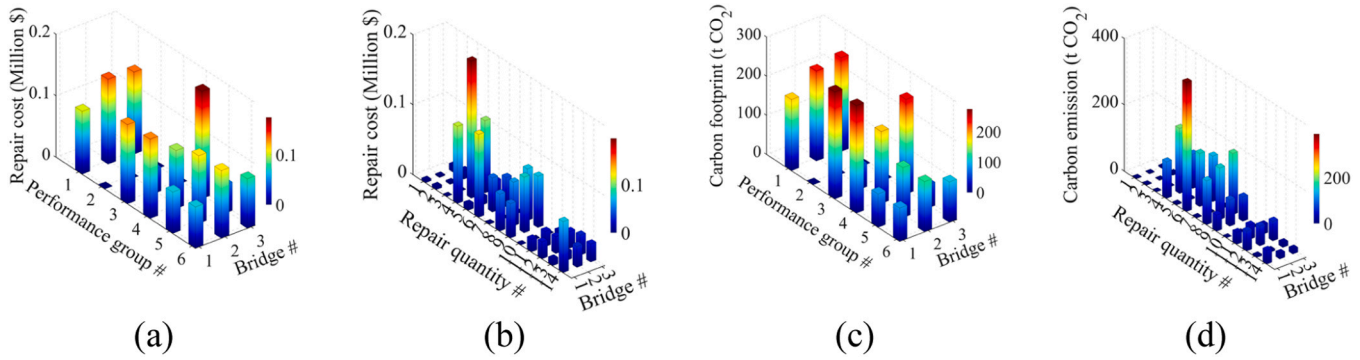

Fig. 19. Disaggregation at SRSS PGA = 1.26 g: (a), (b) Repair cost; (c), (d) carbon emission;.

across diverse bridge configurations. Overall, this framework serves as an efficient and practical tool for decision-makers, providing valuable insights to enhance seismic resilience, optimize sustainability metrics, and improve recovery strategies for critical infrastructure in earthquake-prone regions. The primary conclusions and key insights derived from this study are as follows:

1) The FE model is validated against experimental data from an RC column test, demonstrating its capability to accurately capture nonlinear behavior under cyclic loading. This validation provides a solid foundation for the framework's subsequent application in the rapid assessment of seismic performance, resilience, and post-earthquake losses.
2) It is shown that the seismic resilience and post-earthquake losses show strong dependence on the shaking intensity. Generally, higher SRSS PGA leads to increased repair costs, carbon emissions, and repair time, while seismic resilience decreases sharply, highlighting the challenges of maintaining functionality under severe seismic events.
3) Among six ML models evaluated, the ANN is identified as the best-performing model, consistently achieving the highest R^2 values for seismic resilience prediction, along with the lowest RMSE and MAE. As such, the ANN is implemented as the most reliable and accurate ML model for predicting seismic resilience and post-earthquake losses in the proposed framework.
4) Feature importance analysis reveals that longitudinal gap dominates at low shaking intensities, while column height becomes critical at higher intensities. Smaller gaps and taller columns are associated with higher repair costs, greater carbon emissions, and reduced resilience, highlighting the need to prioritize these attributes in bridge design to enhance performance and minimize environmental impacts during seismic events.
5) Different performance groups (PGs) and repair quantities contribute differently to the overall repair costs and environmental impacts, depending on the extent of damage sustained and structural configuration. This underscores the need for customized retrofit and repair strategies tailored to bridge-specific vulnerabilities to enhance sustainability and resilience outcomes.

CRediT authorship contribution statement

Yewei Zheng: Writing – review & editing, Supervision. **Zilan Zhong:** Resources, Funding acquisition. **Xiao Li:** Formal analysis, Data curation. **Zhijian Qiu:** Writing – original draft, Methodology, Investigation, Formal analysis, Conceptualization.

Declaration of Competing Interest

The authors confirm that they do not possess any financial or personal associations that could have impacted the findings presented in this paper. Furthermore, they do not have any known competing interests.

Acknowledgments

The research is supported by the National Natural Science Foundation of China (Grant No. 52208371 and 52478358), National Key R&D Program of China (Grant No. 2022YFC3080400), the Fundamental Research Funds for Central Universities (Grant No. 20720230073), and the Foundation of Key Laboratory of Urban Security and Disaster Engineering (Beijing University of Technology), Ministry of Education (No. 2024B10).

Data availability

Data will be made available on request.

References

[1] Akbarnezhad M, Salehi M, DesRoches R. Application of machine learning in seismic fragility assessment of bridges with SMA-restrained rocking columns. Structures 2023;50:1320–37.
[2] Akiyama M, Frangopol DM, Ishibashi H. Toward life-cycle reliability-, risk-and resilience-based design and assessment of bridges and bridge networks under independent and interacting hazards: emphasis on earthquake, tsunami and corrosion. Struct Infrastruct Eng 2020;16(1):26–50.
[3] Alipour A, Shafei B. Seismic resilience of transportation networks with deteriorating components. J Struct Eng 2016;142(8):4015015.
[4] Almutairi AS. Seismic response and performance-based assessment of multi-span bridge-ground systems. PhD Thesis, Department of Civil Engineering. San Diego, La Jolla, California: University of California; 2019.
[5] Ataei N, Padgett JE. Fragility surrogate models for coastal bridges in hurricane prone zones. Eng Struct 2015;103:203–13.
[6] Aviram A, Mackie KR, Stojadinovic B. Effect of abutment modeling on the seismic response of bridge structures. Earthq Eng Eng Vib 2008;7(4):395–402.
[7] Biondini F, Camnasio E, Titi A. Seismic resilience of concrete structures under corrosion. Earthq Eng Struct Dyn 2015;44(14):2445–66.
[8] Bruneau M, Chang SE, Eguchi RT, Lee GC, O'Rourke TD, Reinhorn AM, Shinozuka M, Tierney K, Wallace WA, Von Winterfeldt D. A framework to quantitatively assess and enhance the seismic resilience of communities. Earthq Spectra 2003;19(4):733–52.
[9] Caltrans SDC. Caltrans Seismic Design Criteria, Version 1.6. Sacramento, California: California Department of Transportation; 2010.
[10] Chen M, Mangalathu S, Jeon JS. Machine learning–based seismic reliability assessment of bridge networks. J Struct Eng 2022;148(7):06022002.
[11] Cheok GS. Behavior of 1/6-scale model bridge columns subjected to inelastic cyclic loading. Struct J 1990;87(6):630–8.
[12] Chirdeep NR, Gangwar M, Shekhar S, Bahurudeen A. "Seismic resilience of deteriorating bridges under changing climatic conditions.". Eng Struct 2025;324:119355.
[13] Cimellaro GP, Reinhorn AM, Bruneau M. Framework for analytical quantification of disaster resilience. Eng Struct 2010;32(11):3639–49.
[14] CMU. Economic Input-Output Life Cycle Assessment (EIO-LCA) US 2002 (428 sectors) Producer model. Carnegie Mellon University Green Design Institute; 2013. ⟨http://www.eiolca.net/⟩.
[15] Collings D. The carbon footprint of bridges. Struct Eng Int 2021:1–6.
[16] Cornell AC, Jalayer F, Hamburger RO. Probabilistic basis for 2000 SAC federal emergency management agency steel moment frame guidelines. J Struct Eng 2002;128(4):526–32.
[17] Cubrinovski M, Haskell J, Winkley A, Robinson K, Wotherspoon L. Performance of bridges in liquefied deposits during the 2010–2011 Christchurch, New Zealand, earthquakes. J. Perform. Constr. Facil. 2014;28(1):24–39.
[18] Decò A, Bocchini P, Frangopol DM. A probabilistic approach for the prediction of seismic resilience of bridges. Earthq Eng Struct Dyn 2013;42(10):1469–87.
[19] Dong Y, Frangopol DM. Risk and resilience assessment of bridges under mainshock and aftershocks incorporating uncertainties. Eng Struct 2015;83:198–208.
[20] Du A, Padgett JE. Investigation of multivariate seismic surrogate demand modeling for multi-response structural systems. Eng Struct 2020;207:110210.
[21] Elgamal A, Yan L, Yang Z, Conte JP. Three-dimensional seismic response of Humboldt Bay bridge-foundation-ground system. J Struct Eng 2008;134(7):1165–76.
[22] Forcellini D. A 3-DOF system for preliminary assessments of the interaction between base isolation (BI) technique and soil structure interaction (SSI) effects for low-rise buildings. Structures 2024;59:105803.
[23] Forcellini D, Mitoulis SA. Effect of deterioration on critical infrastructure resilience–framework and application on bridges. Results Eng 2025;25:103834.
[24] Frangopol DM, Liu M. Maintenance and management of civil infrastructure based on condition, safety, optimization, and life-cycle cost. Struct Infrastruct Syst 2019:96–108.
[25] Gidaris I, Padgett JE, Barbosa AR, Chen S, Cox D, Webb B, Cerato A. Multiple-hazard fragility and restoration models of highway bridges for regional risk and resilience assessment in the United States: state-of-the-art review. J Struct Eng 2017;143(3):04016188.
[26] Gupta A, Krawinkler H. Estimation of seismic drift demands for frame structures. Earthq Eng Struct Dyn 2000;29(9):1287–305.
[27] Han Q, Du X, Liu J, Li Z, Li L, Zhao J. Seismic damage of highway bridges during the 2008 Wenchuan earthquake. Earthq Eng Eng Vib 2009;8(2):263–73.
[28] Hazus, Federal Emergency Management Agency (F.E.M.A.). (2022). "Hazus Earthquake Model Technical Manual-Hazus 5.1." *Federal Emergency Management Agency*: Washington, DC, USA.
[29] Huang C, Huang S. Seismic resilience assessment of aging bridges with different failure modes. Structures 2021;33:3682–90.
[30] Huang B, Zhu B, Cui S, Duan L, Zhang J. Experimental and numerical modelling of wave forces on coastal bridge superstructures with box girders, Part I: Regular waves. Ocean Eng 2018;149:53–77.
[31] Kiani J, Camp C, Pezeshk S. "On the application of machine learning techniques to derive seismic fragility curves.". Comput Struct 2019;218:108–22.
[32] Lei X, Feng R, Dong Y, Zhai C. Bayesian-optimized interpretable surrogate model for seismic demand prediction of urban highway bridges. Eng Struct 2024;301:117307.
[33] Li Y, Dong Y, Frangopol DM, Gautam D. Long-term resilience and loss assessment of highway bridges under multiple natural hazards. Struct Infrastruct Eng 2020;16(4):626–41.

[34] Liu Z, Sextos A, Guo A, Zhao W. ANN-based rapid seismic fragility analysis for multi-span concrete bridges. Structures 2022;41:804–17.
[35] Loh CH, Tsay CY. Responses of the earthquake engineering research community to the Chi-Chi (Taiwan) earthquake. Earthq Spectra 2001;17(4):635–56.
[36] Lu J, Mackie KR, Elgamal A, Almutairi A. BridgePBEE: OpenSees 3D pushover and earthquake analysis of single-column 2-span bridges. Use Man Beta 2018;1(2).
[37] Luco, N. (2001). Probabilistic seismic demand analysis, SMRF connection fractures, and near source effects. *Ph.D. Dissertation*. Dept. of Civil and Environmental Engineering, Stanford University, California.
[38] Mackie KR, Kucukvar M, Tatari O, Elgamal A. Sustainability metrics for performance-based seismic bridge response. J Struct Eng 2016;142(8):4015001.
[39] Mangalathu S, Heo G, Jeon JS. Artificial neural network based multi-dimensional fragility development of skewed concrete bridge classes. Eng Struct 2018;162:166–76.
[40] Mangalathu S, Hwang SH, Choi E, Jeon JS. Rapid seismic damage evaluation of bridge portfolios using machine learning techniques. Eng Struct 2019;201:109785.
[41] Mangalathu S, Jeon JS. Stripe-based fragility analysis of multispan concrete bridge classes using machine learning techniques. Earthq Eng Struct Dyn 2019;48(11):1238–55.
[42] McKenna F, Scott MH, Fenves GL. Nonlinear finite-element analysis software architecture using object composition. J Comput Civ Eng 2009;24(1):95–107.
[43] Navarro IJ, Penadés-Plà V, Martínez-Muñoz D, Rempling R, Yepes V. Life cycle sustainability assessment for multi-criteria decision making in bridge design: a review. J Civ Eng Manag 2020;26:690–704.
[44] Onat NC, Kucukvar M. Carbon footprint of construction industry: a global review and supply chain analysis. Renew Sustain Energy Rev 2020;124:109783.
[45] Padgett JE, Nielson BG, DesRoches R. Selection of optimal intensity measures in probabilistic seismic demand models of highway bridge portfolios. Earthq Eng Struct Dyn 2008;37(5):711–25.
[46] Pang Y, Wei K, Yuan W. Life-cycle seismic resilience assessment of highway bridges with fiber-reinforced concrete piers in the corrosive environment. Eng Struct 2020;222:111120.
[47] Qiu Z, Prabhakaran A, Ebeido A, Zheng Y. Seismic resilience assessment of sheet-pile wharves in liquefiable soils using different liquefaction countermeasures. Comput Geotech 2024;176:106750.
[48] Qiu Z, Prabhakaran A, Lu J, Elgamal A, Zheng Y. Sustainability and resilience assessment of a reinforced concrete bridge subjected to liquefaction-induced lateral spreading. J Geotech Geoenviron Eng 2024;150(4):04024016.
[49] Qiu Z, Prabhakaran A, Su L, Zheng Y. Performance-based seismic resilience and sustainability assessment of coastal RC bridges in aggressive marine environments. Ocean Eng 2023;279:114547.
[50] Qiu Z, Yu Z, Su L, Prabhakaran A, Elgamal A, Wang X. Longitudinal seismic fragility assessment of an integral bridge-ground system in liquefaction-induced lateral spreads. Soil Dyn Earthq Eng 2023;168:107838.
[51] Rachedi M, Matallah M, Kotronis P. Seismic behavior & risk assessment of an existing bridge considering soil-structure interaction using artificial neural networks. Eng Struct 2021;232:111800.
[52] Scott M, Fenves G. Plastic hinge integration methods for force-based beam-column elements. J Struct Eng 2006;132(2):244–52.
[53] Soleimani F, Hajializadeh D. Bridge seismic hazard resilience assessment with ensemble machine learning. Structures 2022;38:719–32.
[54] Soleimani F, Liu X. Artificial neural network application in predicting probabilistic seismic demands of bridge components. Earthq Eng Struct Dyn 2022;51(3):612–29.
[55] UNEP). (2021). Global status report for buildings and construction: towards a zero-emission. United Nations Environment Programme: Nairobi, Kenya.
[56] Verdugo R, Sitar N, Frost JD, Bray JD, Candia G, Eldridge T, Hashash Y, Olson SM, Urzua A. Seismic performance of earth structures during the February 2010 Maule, Chile, earthquake: dams, levees, tailings dams, and retaining walls. Earthq Spectra 2012;28:75–96.
[57] Vijayakumar M, Cheng JJ, Küçükvar M, Elgamal A, Mackie KR, Tatari O. Carbon footprint: liquefaction effects on a private residence. GeoChic 2016:633–42.
[58] Wang X, Li Z, Shafieezadeh A. Seismic response prediction and variable importance analysis of extended pile-shaft-supported bridges against lateral spreading: exploring optimized machine learning models. Eng Struct 2021;236:112142.
[59] Wang X, Mazumder RK, Salarieh B, Salman AM, Shafieezadeh A, Li Y. Machine learning for risk and resilience assessment in structural engineering: progress and future trends. J Struct Eng 2022;148(8):03122003.
[60] Wang X, Ye A, Ji B. Fragility-based sensitivity analysis on the seismic performance of pile-group-supported bridges in liquefiable ground undergoing scour potentials. Eng Struct 2019;198:109427.
[61] Wang X, Ye A, Yang D, Wu X, Zhou L, Song K, Li J, Peng J, Lou L, Wei X. Component restoration models of highway bridges for resilience assessment: a nationwide expert-opinion survey study and application. Earthq Spectra 2024.
[62] Xu JG, Feng DC, Mangalathu S, Jeon JS. Data-driven rapid damage evaluation for life-cycle seismic assessment of regional reinforced concrete bridges. Earthq Eng Struct Dyn 2022;51(11):2730–51.
[63] Yuan J, Wang Y, Zhan B, Yuan X, Wu X, Ma J. Comprehensive investigation and analysis of liquefaction damage caused by the M_s 7.4 Maduo earthquake in 2021 on the Tibetan Plateau, China. Soil Dyn Earthq Eng 2022;155:107191.
[64] Zhang W, Wen J, Dong H, Han Q, Du X. Post-earthquake functionality and resilience prediction of bridge networks based on data-driven machine learning method. Soil Dyn Earthq Eng 2025;190:109127.
[65] Zhou L, Alam MS, Dong Y, Feng R. Seismic resilience assessment of extended pile shaft supported coastal bridges considering scour and uniform corrosion effects. Eng Struct 2024;304:117643.
[66] Zhou C, Xie Y, Wang W, Zheng Y. Machine learning driven post-impact damage state prediction for performance-based crashworthiness design of bridge piers. Eng Struct 2023;292:116539.